


## Power-Source-Free Analysis of Pyroelectric Energy Conversion

Chenbo Zhang (张晨波),<sup>1</sup> Yintao Song (宋寅韬),<sup>2</sup> Maike Wegner,<sup>3</sup> Eckhard Quandt,<sup>3</sup> and Xian Chen (陈弦)<sup>1,\*</sup>

<sup>1</sup>*Department of Mechanical and Aerospace Engineering, Hong Kong University of Science and Technology, Clear Water Bay, Hong Kong*

<sup>2</sup>*1170 Foster City Boulevard, Foster City, California 94404, USA*

<sup>3</sup>*Faculty of Engineering, University of Kiel, 24143 Kiel, Germany*

 (Received 25 November 2018; revised manuscript received 26 April 2019; published 31 July 2019)

We analyze pyroelectric energy conversion using a power-source-free characterization method, which can also be used to demonstrate electricity generation. In contrast to conventional pyroelectric-energy-conversion designs, our energy system is detached from any external power sources, operating only under periodically varying temperature. Such detachment unambiguously attributes the converted electricity to the heat that drives the change of polarization in the pyroelectric material, not to the electric field alternation caused by the external battery. We demonstrate electricity generation in consecutive temperature cycles by using three phase-transforming ferroelectric materials with different properties. In-depth thermodynamics analysis suggests that the work output is rate dependent: the work output per cycle is linearly dependent on the heating and/or cooling frequency below a predicted threshold. The linearity is confirmed by experiments, and the threshold frequency is derived by theory. Finally, we propose a figure of merit that separates the material's intrinsic properties from the system design parameters. The figure of merit guides future material development and device improvement. Our work clarifies confusions and forms the foundation for the resurgence of pyroelectric material as a competitor for green electricity.

DOI: [10.1103/PhysRevApplied.12.014063](https://doi.org/10.1103/PhysRevApplied.12.014063)

### I. INTRODUCTION

According to the 2008 annual report of U.S. Department of Energy, one third to a half of industrial energy input is wasted as heat of temperature around the boiling point of water [1]. Recycling such low-grade waste heat and integrating it for power generation have a great impact on both the environment and the economy. By far, thermoelectrics, as the most-successful devices directly harvesting power from heat, have dominated applications in this area [2,3]. However, their efficiency and work output density are hindered by the small  $ZT$  [the thermoelectric figure of merit (FOM)] values in the low-temperature regime [4,5]. A recently emerging branch of methods for direct energy conversion from heat is to manipulate the caloric effect by means of one of the multiferroic properties; for example, the pyroelectric effect of ferroelectric materials [6] and the magnetocaloric effect of ferromagnetic materials [7,8]. Generally, the magnetoelectric properties of a material are sensitive to changes in the lattice parameters due to, for example, heating and cooling. This mechanism underlies the temperature-dependent ferroic properties. When

these temperature-dependent ferroic properties are coupled with a structural phase transformation, the caloric effects are dramatically amplified [9–12], which makes energy-harvesting applications admissible and practical.

For ferroelectric materials, a large pyroelectric effect is commonly observed during a structural transformation between the ferroelectric phase and the paraelectric phase. In most cases, such a structural transformation is martensitic; that is, a diffusionless solid-solid reversible phase transformation. As a result, within a narrow temperature range, the polarization of the material exhibits an abrupt jump. State-of-the-art technologies for fabricating sophisticated devices have demonstrated promising pyroelectric properties that can be leveraged by this kind of energy harvesting [6,13]. For example, within a 10-K temperature range, the polarization jump  $[[P]]$  is  $6 \mu\text{C}/\text{cm}^2$  in single-crystal  $\text{BaTiO}_3$  [10] and  $5.5 \mu\text{C}/\text{cm}^2$  in ferroelectric  $\text{Pb}(\text{Mg},\text{Nb})\text{-}0.32\text{PbTiO}_3$  thin films [6]. These materials are good candidates for such an energy-harvesting device.

The first pyroelectric energy device was designed as a capacitor. The working mechanism is based on the different kinds of quasistatic thermodynamic cycles proposed in the early 1980s [14]. Among them, the Ericsson cycle, also known as the Olsen cycle in the pyroelectric literature, has the maximum energy output converted directly from

\*xianchen@ust.hk

heat [15]. In this device, the dielectric layer of the capacitor is made of a phase-transforming ferroelectric material that generates electric current due to the change of polarization when being heated across the phase transformation. With use of the Ericsson cycle, the relationships between the pyroelectric properties and the energy-harvesting performance were widely studied in various ferroic material systems [6,13–16].

An Ericsson cycle consists of two isothermal processes at temperatures below and above the transition temperature and two isobaric processes under different applied electric fields. Energy conversion by the pyroelectric effect utilizing the Ericsson cycle has been demonstrated in many material systems with similar designs [6,13,15]. The common idea of these designs is to connect the pyroelectric capacitor to a load resistor and a battery in series. The load resistor serves as an electricity consumer, across which the changes in voltage and current are considered as the energy harvested from the device. The role of the battery is to provide the device with a bias voltage that controls the change in applied field during the cycles. During the isothermal process at low temperature, the device is in the ferroelectric phase spontaneously polarized by the applied bias voltage. Under constant the electric field, the device is heated up through the transformation temperature, and simultaneously its capacitance jumps due to the phase transition. As a result, the capacitor releases charges passing through the resistor and generates electricity. The measure of the voltage on the load resistor connected to the capacitor is commonly considered as the energy harvested during the heating process [6,13]. At the end of the phase transformation, either the system goes through a symmetric cooling half cycle or the resistor is short-circuited by a diode and then the system is restored to its original state through isothermal discharging and isobaric cooling [15].

A typical energy-conversion circuit using the Ericsson cycle is sketched in Fig. 1(a), with the optional diode omitted. Follow-up developments exploited this circuit in their energy-conversion designs [6,13,15,16]. However, in these designs the electrostatic energy collected during the phase transformation is often confused with the energy given by the external battery. The bias field from the external battery influences the actual energy output. We demonstrate such an effect using a nontransforming regular capacitor in the conventional design, and simply toggle the power-source voltage between 10 and 30 V. As expected, we observe an electricity signal corresponding to the switching of the bias field as shown in Fig. 1(b). The magnitude of this signal depends on the external power source, and is usually much larger than that caused by the pyroelectric effect. In particular, electricity signals observed in the isothermal processes are subjected to the bias field, which should not be considered as the power generated from heat. However, the influence of such signals is unavoidable in designs that can be charged by an external power

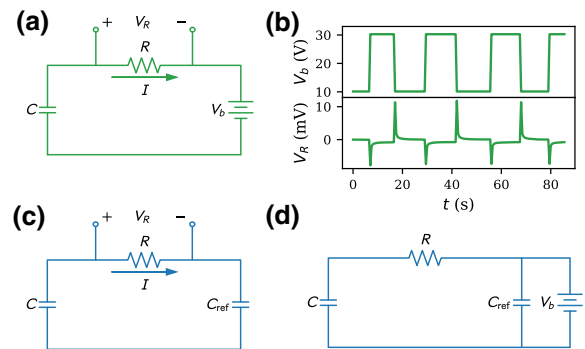


FIG. 1. Conventional and battery-detached pyroelectric-energy-conversion circuits. (a) Conventional design based on Olsen’s design [15]. (b) Demonstration that in the conventional design even using a regular capacitor, simply by varying the battery voltage, one can collect an electricity signal on the resistor, which is clearly not converted from any heat source. (c) Our battery-detached design. (d) Circuit of the one-time initial charging of both capacitors at room temperature before removal of the battery and the start of the cyclic heating and cooling.

source during operation. Motivated by this, we propose a detached pyroelectric apparatus: no external power source is involved throughout the energy-harvesting process by ferroelectric-to-paraelectric transformation thermal cycles.

Another factor often overlooked in thermodynamic analysis of pyroelectric energy conversion is the rate dependency of work output. The modern theoretical framework of thermodynamics is built on top of Carnot’s work [17] for a heat engine. If we compare a common pyroelectric-energy-conversion device with a traditional piston-cylinder heat engine, the energy collected on the load resistor is like the heat generated due to the friction between the piston and the cylinder wall. This type of energy is always considered as dissipation. Therefore, the pyroelectric energy conversion is rate dependent, which is, however, ignored in most classical thermodynamic models. In this paper, we discuss the rate dependency of work output using our power-source-free energy-conversion characterization. By nondimensionalization of the governing equation, we identify a threshold cycling frequency under which the work density varies linearly with the heating and/or cooling rate. To consider the performance, we propose a simple figure of merit by which many coupled design parameters, including material constants, operation conditions, and circuit designs, can be optimized to maximize the work output.

## II. BATTERY-DETACHED PYROELECTRIC ENERGY CONVERSION FROM HEAT TO ELECTRICITY

In our design, we replace the external voltage source in the conventional design by a reference capacitor ( $C_{\text{ref}}$ ) as shown in Fig. 1(c). The thermodynamic role of a capacitor

compared to that of an external power source is different. The former acts as a charge reservoir, which passively receives and releases the charges according to thermally driven phase-transformation cycles. Therefore, the thermodynamic system is a closed system from an electrostatic perspective. Initially, when the temperature of the pyrocapacitor is  $T_L < \theta$ , where  $\theta$  is the phase-transformation temperature, the pyrocapacitor and the reference capacitor are both fully charged to voltage  $V_b$ , so no charges flow in the circuit. This is the initialization of the device shown in Fig. 1(d). Afterward, the external power source is detached throughout the energy-conversion cycles and the total injected charge in the circuit is assumed to be preserved. In practice there will be some charge losses due to leakage, which will not be discussed in this paper. A resistor with resistance  $R$  is connected in series to the pyroelectric capacitor to detect the current generated during the cyclic heating and/or cooling processes. The voltage produced across the resistor is characterized as  $V_R$ . This value will be the index of our energy-conversion circuit as it signals the energy converted purely from the phase transformation. To make the system alternate between  $T_L$  and  $T_H$  cyclically, we maintain two heat reservoirs providing stable temperatures of  $T_L$  and  $T_H$ , respectively. As a proof of concept, the phase transformation is driven by our manually moving the pyroelectric capacitor between the two heat reservoirs.

Let the pyroelectric capacitor be the thermodynamic system. The free charge on its surface is a function of voltage  $V$  and temperature  $T$ , that is,  $Q(V, T)$ , as sketched in Fig. 2. This is regarded as the key physical property responsible for energy conversion. By the charge conservation of the energy-conversion circuit in Fig. 1(c), when the system jumps between the ferroelectric phase and the paraelectric phase, the capacitance of the system alters accordingly, which drives the movement of free charges between the two capacitors. Because  $Q(V_L, T_L) > Q(V_H, T_H)$ , the system will be discharged and/or charged spontaneously during heating and/or cooling processes without any external bias voltage. Unlike the quasistatic thermodynamic cycles assumed by Olsen *et al.* [15], both the voltage and

the temperature of the system vary simultaneously along the heating and/or cooling paths between the two states  $(Q_L, V_L, T_L)$  and  $(Q_H, V_H, T_H)$ , where  $Q_{L,H}$  and  $V_{L,H}$  are the charges and the corresponding voltages of the pyroelectric capacitor in the ferroelectric phase at  $T_L$  and the paraelectric phase at  $T_H$ .

### III. THERMODYNAMIC MODEL

#### A. Governing equation of energy conversion

To have a rational understanding of the relationships among the material intrinsic properties, design parameters, and control parameters of our power-source-free energy-conversion apparatus, we use the electric charge and voltage as the energy conjugate to study the thermodynamics of the system. The dynamics of the charge held by the pyroelectric capacitor is modeled by the time-dependent voltage  $V(t)$  and temperature  $T(t)$ ; that is, at  $t \geq 0$ ,  $Q(t) = Q[V(t), T(t)]$ , with initial voltage  $V(0) = V_b$  and initial temperature  $T(0) = T_L$ . The function  $Q(V, T)$  is a state function that can be determined by the state variables  $V$  and  $T$  despite the time history.

The initial voltage  $V_b$  of the system and the capacitance of the reference capacitor  $C_{\text{ref}}$  determine the total charge in the circuit:

$$Q_{\text{tot}} = C_{\text{ref}}V_b + Q(V_b, T_L). \quad (1)$$

When the system reaches the steady state in the ferroelectric phase at  $T = T_L < \theta$  after being detached from the external power source, the corresponding voltage and charge are the same as in the initial state:

$$V_L = V_b, \quad Q_L = Q(V_b, T_L). \quad (2)$$

On heating, the system transforms from the ferroelectric phase to the paraelectric phase. When the phase transformation finishes, the system reaches the other steady state at  $T = T_H$ . By charge conservation, the corresponding voltage and charge are then

$$V_H = \frac{Q_{\text{tot}} - Q_H}{C_{\text{ref}}}, \quad Q_H = Q(V_H, T_H). \quad (3)$$

In the temperature range  $T_L < T < T_H$ , the charges flow in the circuit due to the change of the capacitance of the system. By Kirchhoff's law of voltage,

$$V = -\dot{Q}(V, T)R + \frac{Q_{\text{tot}} - Q(V, T)}{C_{\text{ref}}}. \quad (4)$$

In Eq. (4),  $R$  denotes the resistance of the resistor across which the output voltage  $V_R = -\dot{Q}(V, T)R$  is used to measure the energy conversion over the cyclic thermal loading.

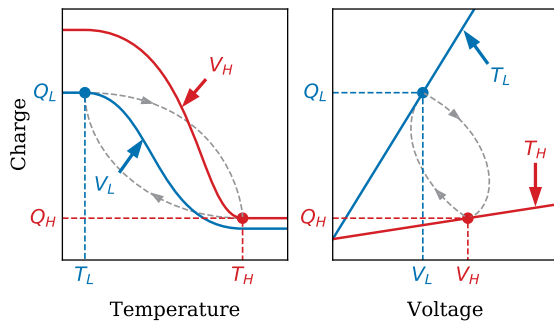


FIG. 2. Thermodynamic states of a pyroelectric capacitor.

$T(t)$  is governed mainly by heat transfer between the system and the heat reservoirs. In our characterization, we can tune  $T(t)$  by manipulating the temperatures of the two reservoirs to achieve different heating and/or cooling rates. In theoretical analysis, we treat them as external stimuli. Then Eq. (4) becomes a first-order nonlinear ordinary differential equation (ODE) for  $V(t)$ :

$$RC_{\text{ref}}\dot{Q} + C_{\text{ref}}V + Q - Q_{\text{tot}} = 0. \quad (5)$$

### B. Change of variables

Using the approximation of a planar capacitor with area  $A$  and thickness  $d$  satisfying  $d \ll \sqrt{A}$ , we estimate the free charge accumulated at the surface of the pyroelectric capacitor as

$$Q(V, T) = \epsilon_0 EA + P(E, T)A, \quad (6)$$

where  $\epsilon_0$  is the vacuum permittivity, and  $E$ , the electric field in the capacitor, is calculated as

$$E = \frac{V}{d}. \quad (7)$$

The constitutive function  $P(E, T)$  is the polarization of the pyroelectric material under the applied electric field  $E$  at temperature  $T$ . This is an intrinsic material property that can be characterized by measuring the  $P$ - $E$  curves at different temperatures [10]. To link the thermodynamic behavior of the system to the material property  $P$ , we change the energy conjugate  $(Q, V)$  to  $(P, E)$ , and the governing equation (5) becomes a first-order nonlinear ODE for the electric field in the pyroelectric material  $E(t)$ . The total charge [Eq. (1)] can be rewritten as

$$Q_{\text{tot}} = C_{\text{ref}}V_b + \frac{\epsilon_0 V_b A}{d} + P_L A, \quad (8)$$

where  $P_L$  represents the polarization of the system in the low-temperature phase; that is ,

$$P_L = P\left(\frac{V_b}{d}, T_L\right). \quad (9)$$

The value of  $P_L$  can be experimentally determined from the  $P$ - $E$  curve at temperature  $T_L$ .

### C. Nondimensionalization of the governing equation

Equation (5) is a nonlinear ODE. It can be numerically integrated. To uncover the intrinsic relationships among coupled parameters, we convert the governing equation into a dimensionless form. We use a bar ( $\bar{\cdot}$ ) to denote dimensionless variables.

If we choose  $V_b$  as the characteristic voltage, then

$$V = V_b \bar{V}, \quad E = \frac{V_b}{d} \bar{E}. \quad (10)$$

We scale the polarization and temperature in the following way:

$$P = P_L \bar{P}, \quad T = \frac{T_H - T_L}{2} \bar{T} + \theta\left(\frac{V_b}{d}\right). \quad (11)$$

Here the function  $\theta(E)$  denotes the transformation temperature under the electric field  $E$ . A closed form is proposed in the discussion of the constitutive assumption in Sec. IV B. In principle, the phase-transformation temperature of a material varies with the application of an external load, which is underlain by the Clausius-Clapeyron relation.

We define the dimensionless charge as

$$Q = P_L A \bar{Q}. \quad (12)$$

If we combine this with Eq. (6), we get

$$\bar{Q} = \frac{\epsilon_0 V_b}{P_L d} \bar{E} + \bar{P}. \quad (13)$$

Finally, time is scaled by

$$t = \tau \bar{t}, \quad (14)$$

in which  $\tau$  is the duration of the heating half cycle. We consider this timescale to be a given constant in our model because it is mostly governed by heat transfer and the thermal properties of the material. As a rough estimate, if the intake heat flow is  $q$  and the latent heat of phase transformation is  $\ell$ , the duration for complete transformation of the material from the low-temperature phase to the high-temperature phase is  $\ell/q$ .

Substituting Eq. (8) into Eq. (5) and nondimensionalizing it, we have

$$\frac{RC_{\text{ref}}}{\tau} \dot{\bar{Q}} + \bar{Q} + \frac{V_b C_{\text{ref}}}{P_L A} (\bar{E} - 1) - \left(\frac{V_b \epsilon_0}{P_L d} + 1\right) = 0. \quad (15)$$

Equation (15) does not assume any particular form of the constitutive response  $\bar{P}(\bar{E}, \bar{T})$ , or equivalently  $P(E, T)$ .

If we solve ODE (15) for  $\bar{E}(\bar{t})$ , then we can reconstruct the dimensional current and the voltage on the resistor as

$$I(t) = -\dot{Q}(t) = -\frac{P_L A}{\tau} \dot{\bar{Q}}, \quad V_R(t) = I(t)R. \quad (16)$$

We assume the duration of the cooling half cycle is also  $\tau$ . The total energy harvested during a full cycle starting at  $t_0$  is

$$\mathcal{W} = \int_{t_0}^{t_0+2\tau} I^2 R dt = \frac{P_L^2 A^2 R}{\tau} \int_{\bar{t}_0}^{\bar{t}_0+2} \dot{\bar{Q}}^2 d\bar{t}. \quad (17)$$

## IV. EXPERIMENTS AND SIMULATION

### A. Energy-conversion demonstration

We prepare three thin-plate specimens: (i) pure  $\text{BaTiO}_3$  with thickness of 0.77 mm and area of  $62.35 \text{ mm}^2$ , (ii)  $\text{BaZr}_{0.006}\text{Ti}_{0.994}\text{O}_3$  with thickness of 0.58 mm and area of  $69.54 \text{ mm}^2$ , and (iii)  $\text{BaZr}_{0.01}\text{Ti}_{0.99}\text{O}_3$  with thickness of 0.57 mm and area of  $33.12 \text{ mm}^2$ . The bulk ceramics are prepared by a conventional solid-state-reaction route. The appropriate amounts of  $\text{BaCO}_3$ ,  $\text{TiO}_2$ , and  $\text{ZrO}_2$  according to the nominal stoichiometry are weighed and mixed with a planetary mill in *n*-hexane with zirconia balls. The weight of the starting agents is controlled to an accuracy of 0.001 g. The calcination of the powders is performed twice at  $1350^\circ\text{C}$ . After each calcination step the samples are ball milled. The powders obtained are mixed with a binding agent and pressed into disks with a diameter of 20 mm. For sintering the pressed disks are surrounded by granulated  $\text{BaTiO}_3$  to obtain a homogeneous temperature distribution within the specimen. The binder is burned out at  $500^\circ\text{C}$  for 1 h, and afterward the temperature is set to  $1500^\circ\text{C}$  for 3 h for the sintering process.

The pyroelectric properties of all three specimens are characterized by an aixACCT TF Analyzer 2000E. At a given temperature, the electric field varies between  $-10$  and  $10 \text{ kV/cm}$  at a frequency of 50 Hz. The value of  $P(E, T)$  is evaluated at the upper branch of the hysteresis loop. [10] As shown in Fig. 3,  $\text{BaZr}_{0.01}\text{Ti}_{0.99}\text{O}_3$  has the largest jump in polarization across the phase transformation. The Zr-doped  $\text{BaTiO}_3$  specimens show bigger  $dP/dT$  than the pure  $\text{BaTiO}_3$ . The ferroelectric-to-paraelectric

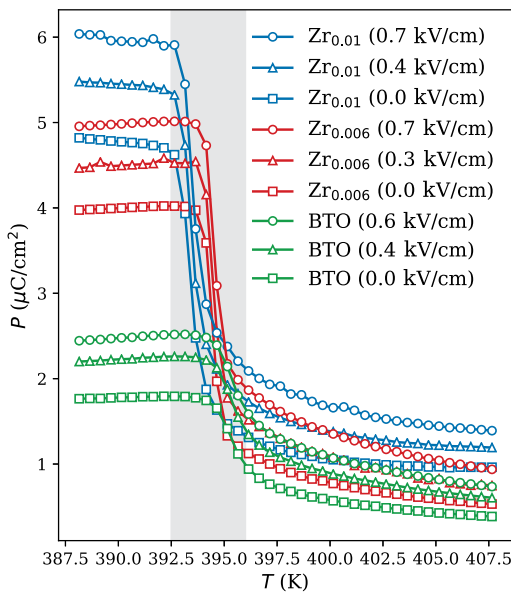


FIG. 3. Pyroelectric behavior of materials. The shaded area indicates the temperature range for phase transformation. BTO,  $\text{BaTiO}_3$ ;  $\text{Zr}_{0.006}$ ,  $\text{BaZr}_{0.006}\text{Ti}_{0.994}\text{O}_3$ ;  $\text{Zr}_{0.01}$ ,  $\text{BaZr}_{0.01}\text{Ti}_{0.99}\text{O}_3$ .

phase transformation in all specimens occurs in the temperature range between  $392.5$  and  $396.0 \text{ K}$ , marked as the shaded area Fig. 3.

At  $t = 0$ , we use a Tektronix PS280 dc power supply to charge the system and achieve equilibrium voltage  $V_b = 30 \text{ V}$ . At  $t > 0$ , the power supply is detached and we monitor the voltage on the resistor while altering the temperature of the system between  $385$  and  $405 \text{ K}$ . Both the temperature and the voltage on resistor are recorded by an Agilent 34970A data acquisition and switch unit. Five consecutive transformation cycles of the system are shown in Fig. 4.

In Fig. 4, we mark the same temperature range for phase transformation as in Fig. 3. Clearly the peaks of the

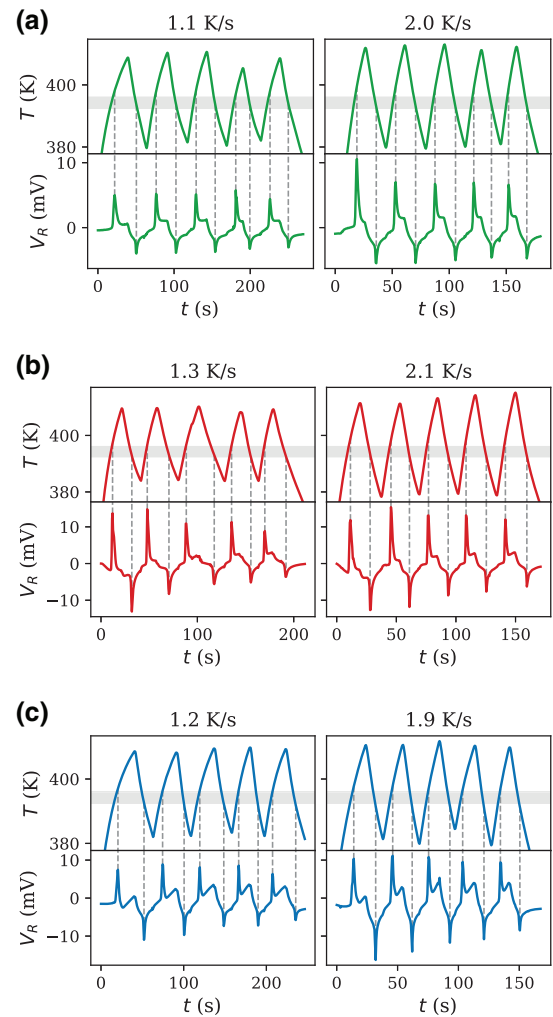


FIG. 4. Voltage generation by the first-order phase transformation in (a)  $\text{BaTiO}_3$ , (b)  $\text{BaZr}_{0.006}\text{Ti}_{0.994}\text{O}_3$ , and (c)  $\text{BaZr}_{0.01}\text{Ti}_{0.99}\text{O}_3$  at two different heating and/or cooling rates. In each plot, upper panels show the cyclic temperature in the specimen, while lower panels show the voltage across the resistor. The shaded temperature ranges in the upper panels are the same ranges as marked in Fig. 3.

electricity signal,  $V_R$ , exactly correspond to the temperature at which phase transformation occurs. This suggests that electricity is generated solely and directly from the phase transformation of the material. Our results are different from the misleading electricity signal measured in a conventional energy-conversion circuit [6], whose peaks coincide with the alternation of the electric field  $E$ .

### B. Constitutive assumption

To solve Eq. (15) numerically, we propose a closed-form constitutive relation  $P(E, T)$ . Consider the case that the giant pyroelectric effect is caused by a first-order phase transformation at temperature  $\theta(E)$ .  $\theta(E)$  is a function of electric field  $E$  due to the Clausius-Clapeyron relation. It corresponds to the center of the decreasing slope in the  $P$ - $E$  curve under the applied field  $E$ . Assuming a linear Clausius-Clapeyron relation,

$$\theta(E) = \theta_0 + \xi E, \quad (18)$$

where  $\xi$  is the Clausius-Clapeyron coefficient.

First, we model the constitutive response for each of the single phases far from the phase-transformation temperature by  $P_f(E)$  and  $P_p(E)$ . Subscripts  $f$  and  $p$  denote the ferroelectric and the paraelectric phase, respectively.  $P_p(E)$  is always linear.  $P_f(E)$  is linear under a small field and approaches a saturated value at high field. Therefore, we use the following hypothesis:

$$P_f(E) = a_f + b_f \tanh(c_f E), \quad (19a)$$

$$P_p(E) = a_p + \chi_p E. \quad (19b)$$

where  $a$ ,  $b$ ,  $c$ , and  $\chi$  are constant coefficients. We define the *jump* of polarization as

$$\llbracket P \rrbracket(E) = P_f(E) - P_p(E). \quad (20)$$

By the shape of constitutive response measured in Fig. 3, we model the function  $P(E, T)$  as

$$P(E, T) = -\llbracket P \rrbracket(E)g[z(E, T)] + P_f(E), \quad (21)$$

where  $\kappa$  is a material constant,  $g(z)$  is the sigmoid function

$$g(z) = \frac{1}{1 + e^{-z}}, \quad (22)$$

and

$$z(E, T) = \frac{4\kappa(T - \theta(E))}{\llbracket P \rrbracket(E)}. \quad (23)$$

Note that  $g(E, T)$  and  $z(E, T)$  are dimensionless.

The constitutive hypothesis [Eq. (21)] has the following properties:

(a) Under any  $E$ ,  $P \rightarrow P_f(E)$  as  $T \rightarrow 0$ , and  $P \rightarrow P_p(E)$  as  $T \rightarrow \infty$ . Across the whole temperature range,  $P$  monotonically decreases from  $P_f(E)$  to  $P_p(E)$ .

(b) Under any  $E$ , the steepest decreasing slope of  $P$ - $T$  occurs at  $\theta(E)$  where the slope is  $-\kappa$ .

(c) We characterize the thermal hysteresis by differential scanning calorimetry. In all test samples, the thermal hysteresis is very small (less than 5 K), which does not have any impact on  $\llbracket P \rrbracket$  and  $\kappa$ . Neither does it contribute to the net electric energy output.

(d) From  $E = 0$ , as  $E$  increases, the  $P$ - $T$  curve shifts to higher temperature (i.e., the Clausius-Clapeyron relation).

Using parameters listed in Table I, we evaluate this hypothetical model and compare it with the experimental measurements for BaTiO<sub>3</sub> in Fig. 5. As shown in Fig. 5, our model captures the temperature dependency of the polarization within the phase-transformation window reasonably well.

After the nondimensionalization described in Sec. III C, we have

$$\bar{P}_f(\bar{E}) = \frac{1}{P_L} \left[ a_f + b_f \tanh\left(\frac{c_f V_b \bar{E}}{d}\right) \right], \quad (24a)$$

$$\bar{P}_p(\bar{E}) = \frac{1}{P_L} \left( a_p + \frac{\chi_p V_b \bar{E}}{d} \right). \quad (24b)$$

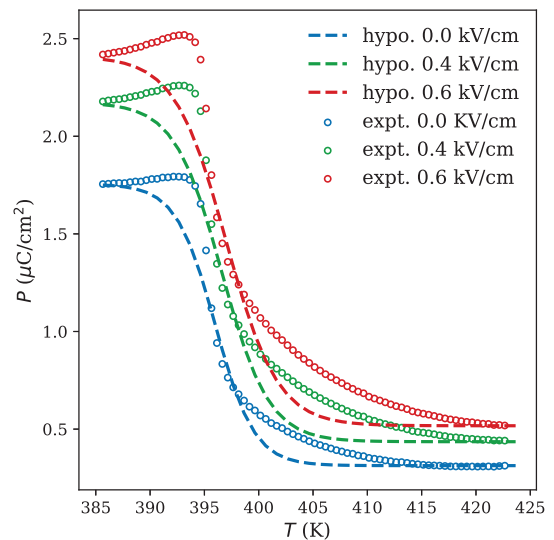


FIG. 5. Temperature dependency of polarization according to our constitutive hypothesis. Open circles represent measurements in BaTiO<sub>3</sub>. Dashed lines correspond the hypothetical model (hypo.) as described by Eq. (21).

We rewrite the dimensionless function  $z(E, T)$  as

$$z(\bar{E}, \bar{T}) = \frac{4\kappa}{P_L \llbracket \bar{P} \rrbracket(\bar{E})} \left( \frac{T_H - T_L}{2} \bar{T} + \frac{\xi V_b}{d} (1 - \bar{E}) \right). \quad (25)$$

The constitutive assumption [Eq. (21)] becomes

$$\bar{P}(\bar{E}, \bar{T}) = -\llbracket \bar{P} \rrbracket(\bar{E})g[z(\bar{E}, \bar{T})] + \bar{P}_f(\bar{E}). \quad (26)$$

### C. Numerical simulation

In the real case,  $T_L$  and  $T_H$  are determined by the target working condition. To demonstrate a simulation of Eq. (15), we let

$$T_L = \theta_0 + \frac{\xi V_b}{d} - 8, \quad (27a)$$

$$T_H = \theta_0 + \frac{\xi V_b}{d} + 2. \quad (27b)$$

That is,

$$\bar{T}_L = -\frac{8}{5}, \quad \bar{T}_H = \frac{2}{5} \quad (28)$$

and  $\bar{T}(\bar{t})$  is defined as

$$\bar{T}(\bar{t}) = -\cos \pi \bar{t} - \frac{3}{10}. \quad (29)$$

Using parameter values in Table I, we integrate Eq. (15) from  $\bar{t} = 0$  to  $\bar{t} = 10$ . The results are compared with experimental measurements in Fig. 6. We show that our model captures the main features of the energy conversion from heat to electricity by the pyroelectric effect. In particular, the peak signals appear exactly at the phase-transition

TABLE I. Parameters used in the simulation.

Variable	Value
$V_b$	30 V
$C_{\text{ref}}$	50 $\mu\text{F}$
$R$	100 k $\Omega$
$A$	60 mm <sup>2</sup>
$d$	0.8 mm
$\theta_0$	396 K
$\kappa$	0.2 $\mu\text{C}/\text{cm}^2 \text{K}$
$\xi$	1.54 K cm/kV
$a_f$	1.7550 $\mu\text{C}/\text{cm}^2$
$b_f$	1.3042 $\mu\text{C}/\text{cm}^2$
$c_f$	0.8643 cm/kV
$a_p$	0.3129 $\mu\text{C}/\text{cm}^2$
$\chi_p$	0.3146 $\mu\text{C}/\text{cm kV}$
$\tau$	10 s

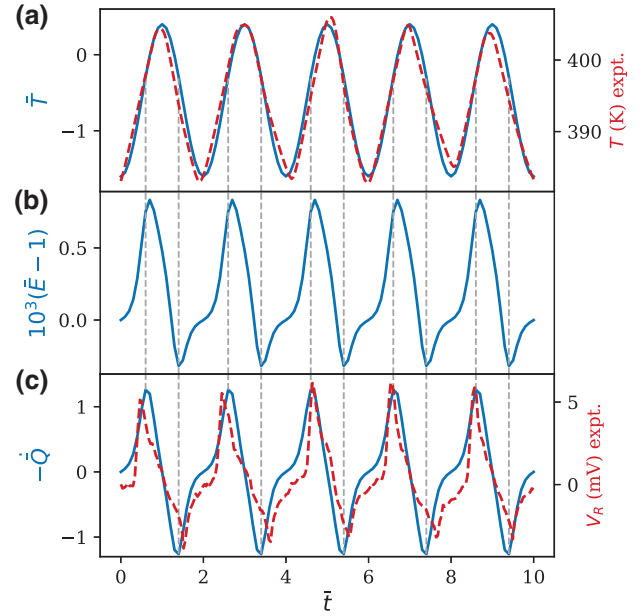


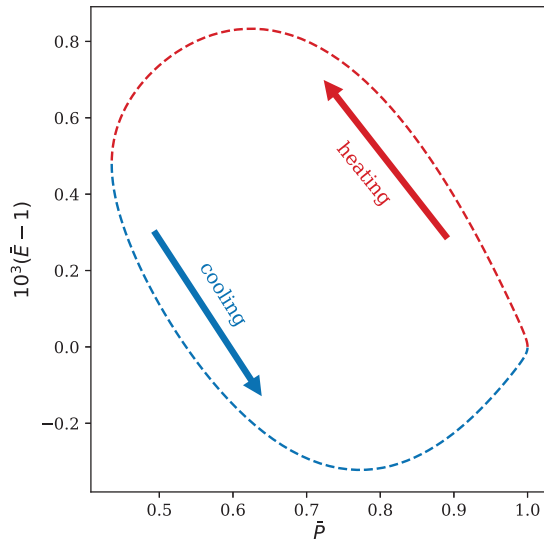
FIG. 6. Simulated dimensionless (a) temperature, (b) field in pyroelectric material, and (c) current flowing through the resistor in five consecutive cycles. Solid blue lines represent simulated results, and dashed red lines represent experimental measurements. Dashed vertical lines indicate peaks in electricity signal,  $-\dot{Q}$ .

temperature. This implies that the collected electricity is directly generated from heat driving the ferroelectric-to paraelectric transition of the active material. In the simulated results in Fig. 6(c), the peak signals for heating and cooling are symmetric, while in the real measurement shown in Fig. 4, the temperature corresponding to the heating peak is higher than that corresponding to the cooling peak. This is because we ignore the hysteresis of the first-order phase transformation in our constitutive hypothesis [Eq. (21)].

We draw the simulated thermodynamic cycle in the  $P$ - $E$  plane in Fig. 7. The work output from the electrostatic work conjugate  $(E, P)$  is compared with the electricity output (17). Here the electrostatic work is computed by

$$\begin{aligned} \mathcal{W}_{\text{ES}} &= Ad \oint -EdP = -Ad \int_{t_0}^{t_0+2\tau} E\dot{P}dt \\ &= -P_L V_b A \int_{\bar{t}_0}^{\bar{t}_0+2} \bar{E}\dot{\bar{P}}d\bar{t}. \end{aligned} \quad (30)$$

Choosing  $\bar{t}_0 = 0$ , we exactly have  $\mathcal{W} = \mathcal{W}_{\text{ES}}$ . One can prove that this equality holds analytically by Eqs. (15), (17), and (30). This means that all the work done by electrostatic force in the pyroelectric material is collected as electricity at the resistor.

FIG. 7. Simulated thermodynamic cycle in the  $P$ - $E$  plane.

## V. FURTHER ANALYSIS

### A. Approximated solution

In this section we analyze the asymptotic limit of pyroelectric energy conversion. The dynamic equation (15) can be converted to an ODE in terms of  $\bar{Q}(\bar{t})$  by changing variables. Then we are able to study the current term  $\dot{\bar{Q}}(\bar{t})$  directly. We expand the Taylor series of  $\bar{Q}(\bar{E}, \bar{T})$  at  $\bar{Q}(1, \bar{T})$ :

$$\bar{Q}(\bar{E}, \bar{T}) = \bar{Q}(1, \bar{T}) + \bar{Q}_{,\bar{E}}(1, \bar{T})(\bar{E} - 1) + \text{higher order terms}, \quad (31)$$

where in  $\bar{Q}_{,\bar{E}}$  the subscript comma denotes a partial derivative. If we ignore higher-order terms, Eq. (15) can be written as a first-order linear ODE for  $\dot{\bar{h}} = \bar{Q}_{,\bar{E}}(1, \bar{T})(\bar{E} - 1)$ :

$$\dot{\bar{h}} + \alpha(\bar{t})\bar{h} + \beta(\bar{t}) = 0, \quad (32)$$

where

$$\alpha(t) = \left(1 + \frac{V_b C_{\text{ref}}}{P_L A \bar{Q}_{,\bar{E}}(1, \bar{T})}\right) \frac{\tau}{RC_{\text{ref}}}, \quad (33a)$$

$$\beta(t) = \dot{\bar{Q}}(1, \bar{T}) + \frac{\tau}{RC_{\text{ref}}} \bar{Q}(1, \bar{T}) - \frac{\tau}{RC_{\text{ref}}} \left(\frac{V_b \epsilon_0}{P_L d} + 1\right) \quad (33b)$$

$$= \bar{P}_{,\bar{T}}(1, \bar{T})\dot{\bar{T}} + \frac{\tau}{RC_{\text{ref}}} [\bar{P}(1, \bar{T}) - 1]. \quad (33c)$$

The ODE (32) can be solved analytically by the integrating-factor method. Here we ignore the detailed

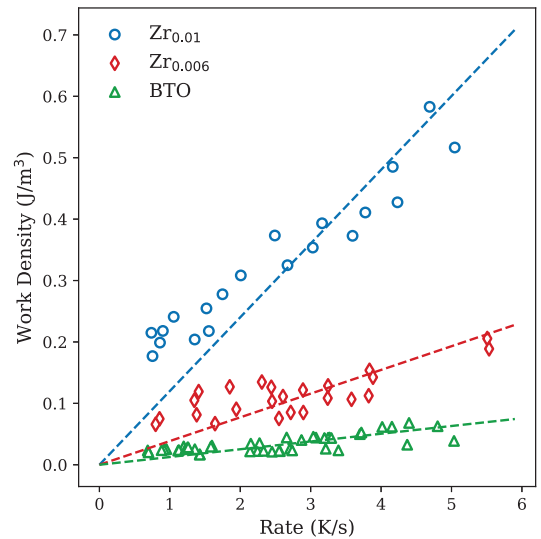


FIG. 8. Work output density per cycle at different heating and/or cooling rates. Each marker corresponds to one cycle from measurements. The first cycles in each measurement are excluded. BTO, BaTiO<sub>3</sub>; Zr<sub>0.006</sub>, BaZr<sub>0.006</sub>Ti<sub>0.994</sub>O<sub>3</sub>; Zr<sub>0.01</sub>, BaZr<sub>0.01</sub>Ti<sub>0.99</sub>O<sub>3</sub>.

solution procedure and focus only on a special degeneracy of the equation.

In Eq. (32), when  $\alpha(t) \gg 1$  and  $\alpha(t) \gg |\beta(t)|$ ,  $\bar{h}$  asymptotically vanishes. Then we can estimate  $\bar{Q}(\bar{E}, \bar{T})$  by  $\bar{Q}(1, \bar{T})$ , which is rate independent. By Eq. (17), the work output scales linearly with frequency:  $\mathcal{W} \propto 1/\tau$ .

For our specimens,  $\alpha$  is on the order of  $10^6$ – $10^7$  and  $|\beta|$  is on the order of 1–10. The rate dependencies of work output per cycle are verified by our power-source-free energy-conversion circuit for three test samples shown in Fig. 8. Compared with state-of-the-art thin-film pyroelectric devices assisted by alternating electric fields [6, 13, 15, 16], the maximum energy density purely converted from heat in the bulk is of the same order of magnitude in BaZr<sub>0.01</sub>Ti<sub>0.99</sub>O<sub>3</sub>.

### B. Threshold frequency

In this section, we derive an estimated criterion under which the asymptotic conditions  $\alpha(t) \gg 1$  and  $\alpha(t) \gg |\beta(t)|$  hold. First, we estimate  $\bar{Q}_{,\bar{E}}(1, \bar{T})$  as

$$\bar{Q}_{,\bar{E}}(1, \bar{T}) = \frac{\epsilon_0 V_b}{P_L d} + \bar{P}_{,\bar{E}}(1, \bar{T}). \quad (34)$$

$\bar{P}_{,\bar{E}}$  comes from two factors: (i) single-phase permittivity and (ii) coupling between the change in permittivity and the Clausius-Clapeyron relation. We denote the ferroelectric susceptibility as  $\chi_f = P'_f(E)$ . By Eq. (19a) we have,  $\chi_f = b_f c_f \cosh^{-2}(c_f E)$ . When  $E$  is not too large,



$\chi_f \approx b_f c_f$ . As  $E \rightarrow \infty$ ,  $\chi_f \rightarrow 0$ . Then we can estimate

$$\bar{Q}_{\bar{E}}(1, \bar{T}) \approx \frac{V_b}{P_L d} (\epsilon_0 + \chi_f + \kappa \xi). \quad (35)$$

That is,

$$\alpha \approx \frac{\tau}{RC_{\text{ref}}} \left( 1 + \frac{C_{\text{ref}} d}{A(\epsilon_0 + \chi_f + \kappa \xi)} \right) \quad (36)$$

and

$$\beta \approx \frac{\kappa(T_H - T_L)}{P_L} + \frac{\tau}{RC_{\text{ref}}}. \quad (37)$$

From Eq. (36), to satisfy  $\alpha \gg 1$ , we need

$$\frac{\tau}{RC_{\text{ref}}} \gg 1 \quad (38)$$

or

$$\frac{d\tau}{RA(\epsilon_0 + \chi_f + \kappa \xi)} \gg 1. \quad (39)$$

By Eq. (37), if Eq. (38) holds, then  $\alpha \gg \beta$  leads to

$$\frac{C_{\text{ref}} d}{A(\epsilon_0 + \chi_f + \kappa \xi)} \gg 1, \quad (40)$$

which is not related to the rate parameter  $\tau$ . If instead we have Eq. (39), then

$$\alpha \gg \beta \implies \frac{C_{\text{ref}} d}{A(\epsilon_0 + \chi_f + \kappa \xi)} \gg \frac{\kappa(T_H - T_L)}{P_L}. \quad (41)$$

We define the threshold frequency to be (the factor 1/10 is chosen as a safety coefficient when we consider the  $\gg$  operator)

$$f^* = \frac{1}{10} \max \left\{ \frac{1}{RC_{\text{ref}}}, \frac{d}{RA(\epsilon_0 + \chi_f + \kappa \xi)} \right\}. \quad (42)$$

When  $1/\tau$  approaches or even exceeds  $f^*$ , the rate-independent approximation  $\bar{Q}(\bar{E}, \bar{T}) = \bar{Q}(1, \bar{T})$  starts to fail.  $\mathcal{W}$  starts to scale only sublinearly with  $1/\tau$ .

From our constitutive model (21) and the parameters in Table I, the threshold frequency  $f^* = 100.6$  Hz. So the rate-independent approximation holds in almost all practical situations. (Also, under a frequency as high as or even higher than 100 Hz, our pure direct-current model may need to be corrected.) However,  $f^*$  will drastically decrease if we use a thin-film geometry, as suggested by Eq. (42). In Fig. 9, we show the simulated rate dependency of dimensionless work output  $\bar{\mathcal{W}}$  for the parameters in Table I and a thin-film alternative with  $d = 200$  nm. For

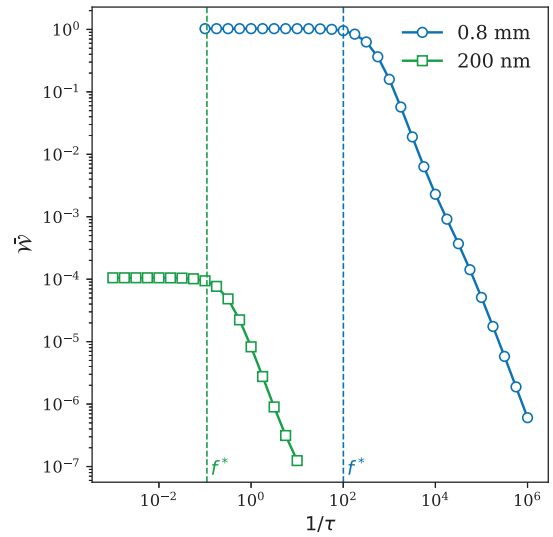


FIG. 9. Simulated rate dependencies in the bulk and thin film. The dimensionless work per cycle  $\bar{\mathcal{W}}$  is evaluated for the tenth cycle at each  $\tau$ .

the thin film, estimated  $f^* = 0.11$  Hz, and the sublinearity occurs at a much lower frequency compared with the bulk version. The dimensionless work output  $\bar{\mathcal{W}}$  in Fig. 9 is defined as

$$\bar{\mathcal{W}} = \int_{\bar{t}_0}^{\bar{t}_0+2} \dot{Q}^2 d\bar{t}. \quad (43)$$

By Eq. (17) it is related to  $\mathcal{W}$  by

$$\mathcal{W} = \frac{P_L^2 A^2 R}{\tau} \bar{\mathcal{W}}. \quad (44)$$

### C. Figure of merit

In this section, we derive a simple estimate for the work output when  $1/\tau$  is well below the threshold frequency; that is, we can use the approximation  $\bar{Q}(\bar{E}, \bar{T}) = \bar{Q}(1, \bar{T})$ . Assuming the heating and cooling half cycles are symmetric, the work output of a full cycle is twice that of the heating half cycle. Because of the dimensionless work [Eq. (43)], in our approximation, it reads

$$\begin{aligned} \bar{\mathcal{W}} &= 2 \int_{\bar{t}_0}^{\bar{t}_0+1} \dot{Q}(1, \bar{T})^2 d\bar{t} = 2 \int_{\bar{t}_0}^{\bar{t}_0+1} \dot{P}(1, \bar{T})^2 d\bar{t} \\ &= 2 \int_{\bar{t}_0}^{\bar{t}_0+1} \dot{P}(1, \bar{T}) \bar{P}_{\bar{T}}(1, \bar{T}) \dot{T} d\bar{t} \\ &= 2 \int_{\bar{T}_L}^{\bar{T}_H} \dot{P}(1, \bar{T}) \bar{P}_{\bar{T}}(1, \bar{T}) d\bar{T}. \end{aligned} \quad (45)$$

$\bar{P}_{\bar{T}}(1, \bar{T})$  is always negative in the temperature range  $[\bar{T}_L, \bar{T}_H]$ . By the mean-value theorem, there exists a value

$\bar{T}_L \leq \gamma \leq \bar{T}_H$  such that

$$\begin{aligned}\bar{\mathcal{W}} &= 2\dot{\bar{P}}(1, \gamma) \int_{\bar{T}_L}^{\bar{T}_H} \bar{P}_{,\bar{T}}(1, \bar{T}) d\bar{T} \\ &= 2\bar{P}_{,\bar{T}}(1, \gamma) \dot{\bar{T}}(\gamma) [\bar{P}(1, T_H) - \bar{P}(1, T_L)].\end{aligned}\quad (46)$$

Up to now, the derivation is exact. Next we estimate each term in Eq. (46):

$$\bar{P}_{,\bar{T}}(1, \gamma) \approx -\frac{\kappa(T_H - T_L)}{2P_L},\quad (47a)$$

$$\dot{\bar{T}}(\gamma) \approx 2,\quad (47b)$$

$$\bar{P}(1, T_H) - \bar{P}(1, T_L) \approx -\llbracket \bar{P} \rrbracket(1).\quad (47c)$$

Substituting (47a), (47b) and (47c) back into Eq. (46) and then to Eq. (17) gives

$$\mathcal{W} \approx \frac{2\kappa \llbracket P \rrbracket A^2 R (T_H - T_L)}{\tau},\quad (48)$$

where  $\llbracket P \rrbracket$  is a short form for the functional evaluation  $\llbracket P \rrbracket(V_b/d)$ , which can be loosely interpreted as “the jump of polarization across the phase transformation”. The work density is then

$$w \approx \frac{2\kappa \llbracket P \rrbracket A R (T_H - T_L)}{d\tau}.\quad (49)$$

Recall, as discussed in Sec. III C, that when the heat flow is predetermined and  $[T_L, T_H]$  covers the whole phase-transformation region,  $\tau \propto \ell$ , where  $\ell$  is the latent heat of the phase transformation. We propose the FOM

$$\zeta = \frac{\kappa \llbracket P \rrbracket A R}{\ell d} := \zeta_1 \zeta_2.\quad (50)$$

Here  $\zeta_1$  is determined by material properties, while  $\zeta_2$  depends on device parameters. The thermal hysteresis of the reversible phase transformation should also be considered as a design factor to ensure the functionality of the pyroelectric material does not degrade over periodic temperature cycles. For BaTiO<sub>3</sub>-based materials, the thermal hysteresis of the phase transformation is around 5 K, which is sufficiently small for cyclic measurement in our setting. For our specimens, the material FOM  $\zeta_1$  is 0.35, 3.5, and 4.0  $\mu\text{C}^2/\text{JcmK}$  for BaTiO<sub>3</sub>, BaZr<sub>0.006</sub>Ti<sub>0.994</sub>O<sub>3</sub>, and BaZr<sub>0.01</sub>Ti<sub>0.99</sub>O<sub>3</sub> respectively, values that agree well with the performance measured at various rates in Fig. 8. If we consider the efficiency estimated as the ratio of the work density and the absorbed heat, an equivalent material FOM can be expressed as  $\kappa \llbracket P \rrbracket / \ell^2$ . Conventionally,

the pyroelectric coefficient  $\kappa = P_{,T}$  is usually used as a critical performance measure of materials used for pyroelectric energy conversion. According to Eq. (50), both the pyroelectric properties and the thermal properties of a material should be considered for material development. However, this does not mean that the second-order phase transformation with much smaller latent heat is superior to the first-order phase transformation. If two materials have the same efficiency, the one with larger latent heat will release more energy during the ferroelectric-to-paraelectric phase transformation. When an energy system concerns only the maximum energy output, the material FOM  $\zeta_1$  is the major factor; for example, BaZr<sub>0.006</sub>Ti<sub>0.994</sub>O<sub>3</sub> and BaZr<sub>0.01</sub>Ti<sub>0.99</sub>O<sub>3</sub> have much better performance than BaTiO<sub>3</sub> in Fig. 8. This result inspires further material research and device engineering to achieve better energy-conversion performance.

## ACKNOWLEDGMENTS

C.Z. and X.C. thank the HK Research Grants Council for financial support under Grants No. 26200316 and No. 16207017. X.C. also thanks the Isaac Newton Institute for Mathematical Sciences for support and hospitality during the program “The Mathematical Design of New Materials,” when work on this paper was undertaken. This work was supported by EPSRC Grant No. EP/R014604/1. E.Q. and M.W. acknowledge funding by the DFG through a Reinhart Koselleck Project (Grant No. QU 146/23-1).

- [1] I. Johnson, W. T. Choate, and A. Davidson, *Waste heat recovery. Technology and opportunities in US industry*, Tech. Rep. (BCS, Inc., Laurel, MD (United States), 2008).
- [2] X. Zhang and L.-D. Zhao, Thermoelectric materials: Energy conversion between heat and electricity, *J. Materials* **1**, 92 (2015).
- [3] L.-D. Zhao, S.-H. Lo, Y. Zhang, H. Sun, G. Tan, C. Uher, C. Wolverton, V. P. Dravid, and M. G. Kanatzidis, Ultralow thermal conductivity and high thermoelectric figure of merit in SnSe crystals, *Nature* **508**, 373 (2014).
- [4] G. Tan, F. Shi, S. Hao, L.-D. Zhao, H. Chi, X. Zhang, C. Uher, C. Wolverton, V. P. Dravid, and M. G. Kanatzidis, Non-equilibrium processing leads to record high thermoelectric figure of merit in PbTe–SrTe, *Nat. Commun.* **7**, 12167 (2016).
- [5] Y. He, T. Day, T. Zhang, H. Liu, X. Shi, L. Chen, and G. J. Snyder, High thermoelectric performance in non-toxic earth-abundant copper sulfide, *Adv. Mater.* **26**, 3974 (2014).
- [6] S. Pandya, J. Wilbur, J. Kim, R. Gao, A. Dasgupta, C. Dames, and L. W. Martin, Pyroelectric energy conversion with large energy and power density in relaxor ferroelectric thin films, *Nat. Mater.* **17**, 432 (2018).
- [7] V. Srivastava, Y. Song, K. Bhatti, and R. James, The direct conversion of heat to electricity using multiferroic alloys, *Adv. Energy Mater.* **1**, 97 (2011).

- [8] Y. Song, K. P. Bhatti, V. Srivastava, C. Leighton, and R. D. James, Thermodynamics of energy conversion via first order phase transformation in low hysteresis magnetic materials, *Energy Environ. Sci.* **6**, 1315 (2013).
- [9] H. Wada and Y. Tanabe, Giant magnetocaloric effect of  $\text{MnAs}_{1-x}\text{Sb}_x$ , *Appl. Phys. Lett.* **79**, 3302 (2001).
- [10] X. Moya, E. Stern-Taulats, S. Crossley, D. González-Alonso, S. Kar-Narayan, A. Planes, L. Mañosa, and N. D. Mathur, Giant electrocaloric strength in single-crystal  $\text{BaTiO}_3$ , *Adv. Mater.* **25**, 1360 (2013).
- [11] X. Moya, S. Kar-Narayan, and N. D. Mathur, Caloric materials near ferroic phase transitions, *Nat. Mater.* **13**, 439 (2014).
- [12] D. Zhao, J. Liu, X. Chen, W. Sun, Y. Li, M. Zhang, Y. Shao, H. Zhang, and A. Yan, Giant caloric effect of low-hysteresis metamagnetic shape memory alloys with exceptional cyclic functionality, *Acta Mater.* **133**, 217 (2017).
- [13] Y. F. Lee, H. R. Jo, C. S. Lynch, and L. Pilon, Pyroelectric energy conversion using PLZT ceramics and the ferroelectric-ergodic relaxor phase transition, *Smart Mater. Struct.* **22**, 025038 (2013).
- [14] R. B. Olsen and D. Evans, Pyroelectric energy conversion: Hysteresis loss and temperature sensitivity of a ferroelectric material, *J. Appl. Phys.* **54**, 5941 (1983).
- [15] R. B. Olsen, D. A. Bruno, and J. M. Briscoe, Pyroelectric conversion cycles, *J. Appl. Phys.* **58**, 4709 (1985).
- [16] G. Sebald, L. Seveyrat, G. Guyomar, L. Lebrun, B. Guiffard, and S. Pruvost, Electrocaloric and pyroelectric properties of  $0.75\text{Pb}(\text{Mg}_{1/3}\text{Nb}_{2/3}\text{O}_3-0.25\text{PbTiO}_3$  single crystals, *J. Appl. Phys.* **100**, 124112 (2006).
- [17] S. Carnot, *Réflexions sur la puissance motrice du feu et sur les machines propres à développer cette puissance* (Bachelier, 1824).